CM² MAGAZINE

第 119 期

南方科技大学海洋磁学中心主编

http://cm2.sustech.edu.cn/

创刊词

海洋是生命的摇篮，是文明的纽带。地球上最早的生命诞生于海洋，海洋里的生命最终进化成了人类，人类的文化融合又通过海洋得以实现。人因海而兴。

人类对海洋的探索从未停止。从远古时代美丽的神话传说，到麦哲伦的全球航行，再到现代对大洋的科学钻探计划，海洋逐渐从人类敬畏崇拜幻想的精神寄托演变成可以开发利用与科学研究的客观存在。其中，上个世纪与太空探索同步发展的大洋科学钻探计划将人类对海洋的认知推向了崭新的纬度：深海（deep sea）与深时（deep time）。大洋钻探计划让人类知道，奔流不息的大海之下，埋藏的却是亿万年的地球历史。它们记录了地球板块的运动，从而使板块构造学说得到证实；它们记录了地球环境的演变，从而让古海洋学方兴未艾。

在探索海洋的悠久历史中，从大航海时代的导航，到大洋钻探计划中不可或缺的磁性地层学，磁学发挥了不可替代的作用。这不是偶然，因为从微观到宏观，磁性是最基本的物理属性之一，可以说，万物皆有磁性。基于课题组的学科背景和对海洋的理解，我们对海洋的探索以磁学为主要手段，海洋磁学中心因此而生。

海洋磁学中心，简称 CM^2，一为其全名“Centre for Marine Magnetism”的缩写，另者恰与爱因斯坦著名的质能方程 $E = MC^2$ 对称，借以表达我们对科学巨匠的敬仰和对科学的不懈追求。

然而科学从来不是单打独斗的产物。我们以磁学为研究海洋的主攻利器，但绝不仅限于磁学。凡与磁学相关的领域均是我们关注的重点。为了跟踪反映国内外地球科学特别是与磁学有关的地球科学领域的最新研究进展，海洋磁学中心特地主办 CM^2 Magazine，以期与各位地球科学工作者相互交流学习、合作共进！

“海洋孕育了生命，联通了世界，促进了发展”。21 世纪是海洋科学的时代，由陆向海，让我们携手迈进中国海洋科学的黄金时代。

目录

1. 海洋和大气变化对最后一个冰期中欧亚大陆冰盖海洋基底的消退影响

翻译人：仲义 zhongy@sustech.edu.cn

Sejrup, H.P., Hjelstuen, B.O., Patton, H., et al., ***The role of ocean and atmospheric dynamics in the marine-based collapse of the last Eurasian Ice Sheet*** *[J] Communications Earth & Environment, 2022, 3(1), 119.*

https://doi.org/10.1038/s43247-022-00447-0

摘要：对过去冰盖演化历史的信息可以为理解现今冰盖受控机制提供重要的背景。作者重建了末次冰消期以来欧亚冰盖历史，强调了挪威海峡和巴伦支海冰川撤退是如何在 18.7 千年导致英国和芬诺斯坎底冰原的分离，以及 16-15 千年间卡拉-巴伦支海和斯瓦尔巴群岛与芬诺斯坎底冰原的分离。结合冰盖模拟和古海洋学数据，作者的重建结果表明，当海平面上升达到最高 20 m 开始，冰川消退主要由南部的温度导致的表面质量平衡以及北部的北欧的海洋环流所驱动的。作者的结果强调出冰盖对外部强迫的非线性特征，以及海洋-海冰-大气动力学变化在现今冰盖变化中的重要性。

ABSTRACT: Information from former ice sheets may provide important context for understanding the response of today's ice sheets to forcing mechanisms. Here we present a reconstruction of the last deglaciation of marine sectors of the Eurasian Ice Sheet, emphasising how the retreat of the Norwegian Channel and the Barents Sea ice streams led to separation of the British Irish and Fennoscandian ice sheets at c. 18.700 and of the Kara-Barents Sea-Svalbard and Fennoscandian ice sheets between 16.000 and 15.000 years ago. Combined with ice sheet modelling and palaeoceanographic data, our reconstruction shows that the deglaciation, from a peak volume of 20 m of sea-level rise equivalent, was mainly driven by temperature forced surface mass balance in the south, and by Nordic Seas oceanic conditions in the north. Our results highlight the nonlinearity in the response of an ice sheet to forcing and the significance of ocean-ice-atmosphere dynamics in assessing the fate of contemporary ice sheets.

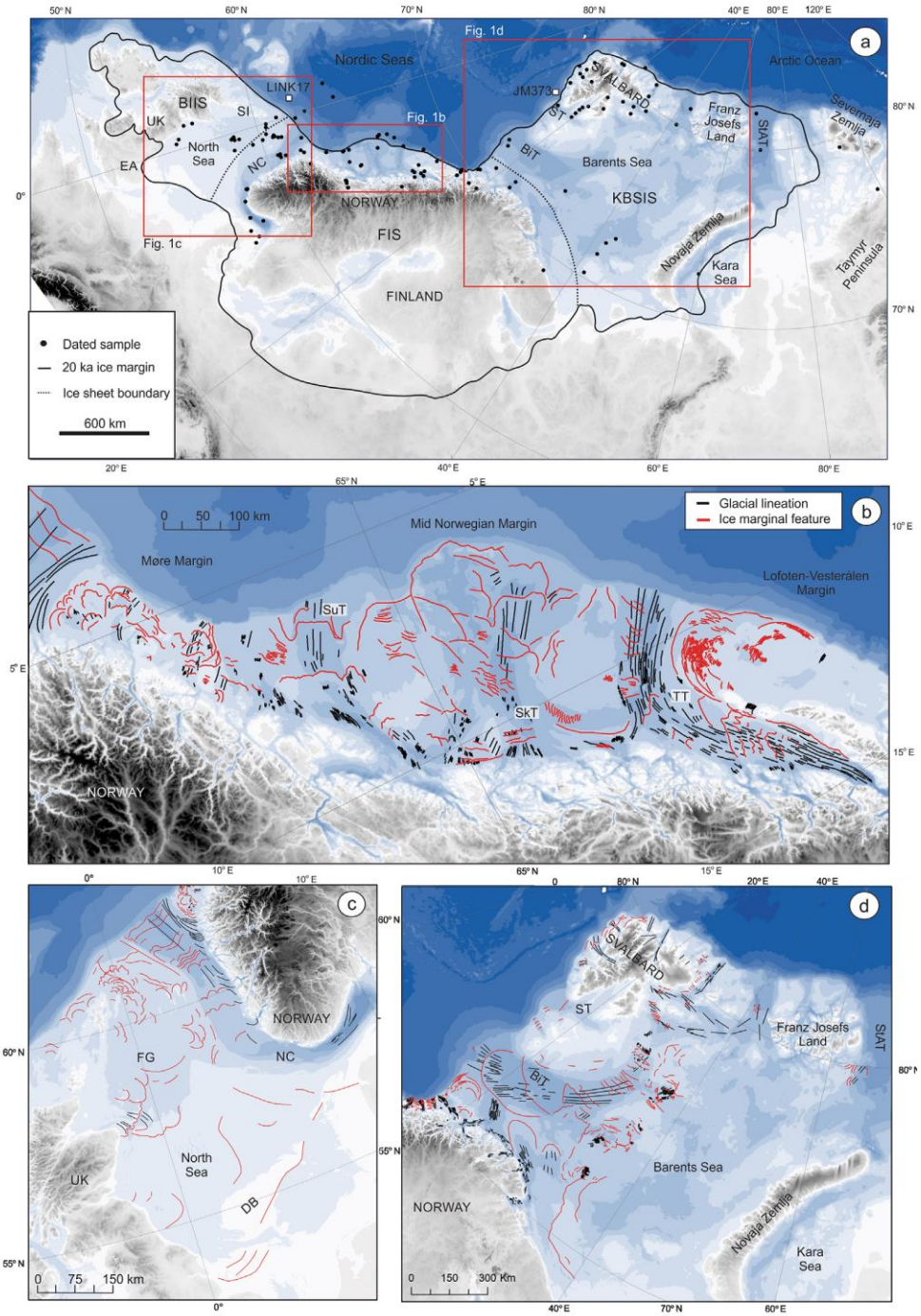

Figure 1. Maps of investigated areas and mapped glacial landforms. a Overview map (bathymetry from www.gebco.net) with Last Glacial Maximum (20 ka) extent (black line) of the Eurasian Ice Sheet and boundaries (broken black lines) between the Kara-Barents Sea-Svalbard Ice Sheet (KBSIS), Fennoscandian Ice Sheet (FIS) and the British-Irish Ice Sheet (BIIS) indicated. Location of deep sea cores (LINK17 and JM373; white squares) and dated samples (Supplementary Note 1 and Supplementary Data 1–3) (black dots) are indicated. b, c Ice marginal features (red lines) and glacial lineations (black lines) mapped on the Mid Norwegian margin and compiled for the North

Sea, largely based on refs. 9,10,12,22. d Ice marginal features (red lines) and glacial lineations (black lines) in the Barents Sea-Svalbard region, compiled using datasets from refs. 32,61,62,67,82,83. NC Norwegian Channel, FG Fladen Ground, DB Dogger Bank, SuT Suladjupet Trough, SkT Sklinnadjupet Trough, TT Trænadjupet Trough, BiT Bjørnøya Trough, ST Storfjorden Trough, StAT St Anna Trough, SI Shetland Islands, EA East Anglia.

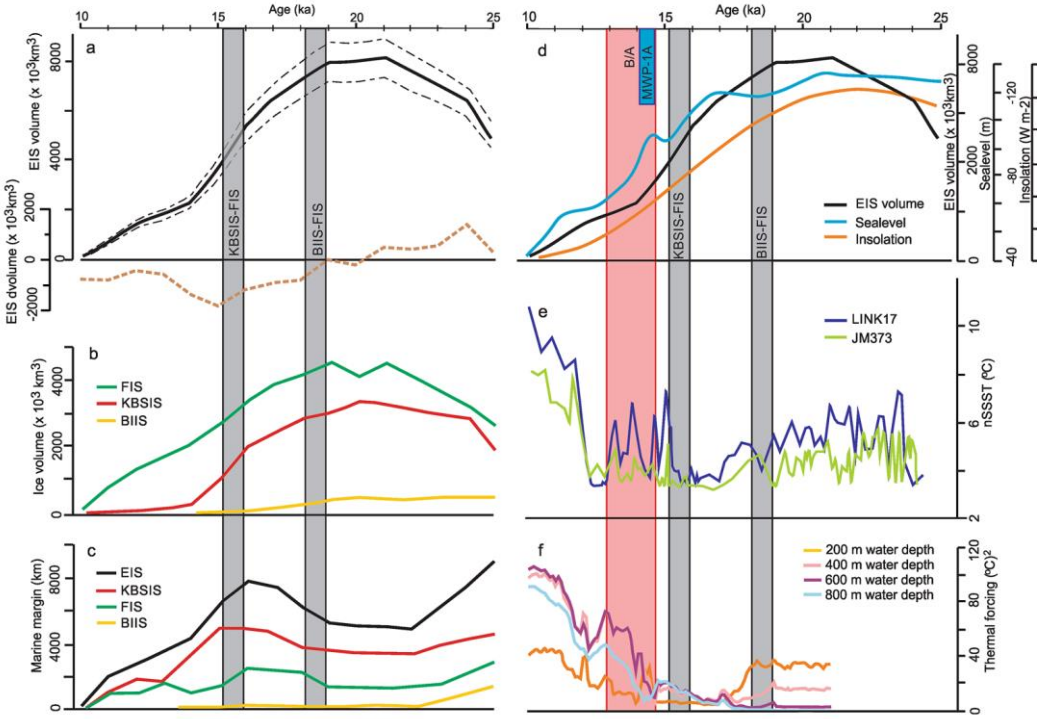

Figure 2. Time series of Eurasian Ice Sheet development and possible controlling factors for the period 25 to 10 ka. a Ice volume of the EIS (black line), model run with shear stress values by ±20% (broken black lines) and volume change in thousand km3 (broken brown line). b Ice volume of the FIS (green line), KBSIS (red line), and BIIS (yellow line) in km^3. c Length of marine margin in km (colour coding as in a, b). d Summer insolation at 65°N in Wm-284 (orange line), EIS volume in thousand km3 (black line) and global sea level85 (blue line). e Summer sea surface temperature estimates based on planktonic foraminifera assemblages from two deep sea cores, Link 17 and JM373. f Modelling of eastern Nordic Seas ocean temperatures36. Grey columns indicate the millennium for break-up of the Eurasian Ice Sheet (EIS) into the Kara-Barents Sea Ice Sheet (KBSIS), Fennoscandian Ice Sheet (FIS) and British-Irish Ice Sheet (BIIS). Red column indicate the Bølling-Allerød (B/A) time period and Meltwater Pulse-1A (MWP-1A) are indicated with a blue box.

2. 利用高温磁化率仪器进行差热分析

翻译人：张琪 zhangq7@sustech.edu.cn

Doctor R, Feinberf J. M, ***Differential thermal analysis using high temperature susceptibility instruments*** *[J]. Journal of Geophysical Research: Solid Earth, 2022, e2021JB023789.*

https://doi.org/10.1029/2021JB023789

摘要：测量磁化率与温度的函数关系是定量样品磁性矿物的一个重要且标准的方法。这些测量用于确定组成矿物的 Curie/Néel 温度，并能够提供热诱导氧化和磁性矿物生成的证据。因此，高温磁化率桥(HTSB)是世界各地古地磁实验室常用的仪器。 本文作者认为 HTSBs 可以用于进行简单的差热分析(DTA)，一种通过测量温度和稳态加热速率的的偏差来测量相变相变和释放/吸收热反应的技术。由于 HTSBs 被设计用来以相对恒定的速率加热样品，因此标准磁化率测量可以用来获得类似相变的信息。作者对蓝铁矿，针铁矿和磁赤铁矿的标准样品和空白样品的加热曲线进行比较，用来确定类似 DTA 的信息。 对于针铁矿和蓝铁矿所确定的反应在磁化率上没有相应的体现，这表明此方法放大了这种常见设备的功能。作者估算了可检测反应的最小焓值和它们的质量关系。此外，本文表明，这种方法能够在混杂自然矿物样品中成功地检测到脱水蓝铁矿。

ABSTRACT: Measurements of susceptibility as a function of temperature are an important, standard method of quantifying a sample's magnetic mineralogy. These measurements are used to identify the Curie/Néel temperatures of constituent minerals and show evidence of thermally-induced oxidation and formation of magnetic minerals. For these reasons, the High Temperature Susceptibility Bridge (HTSB) is a common instrument in paleomagnetism laboratories around the world. Here, we argue that HTSBs can be used to perform simple differential thermal analysis (DTA), a technique used to measure phase transitions and exo-/endothermic reactions by measuring deviations in temperature from a steady heating rate. Because HTSBs are designed to heat samples at a relatively constant rate, the standard susceptibility measurement can be used to obtain similar information, albeit crude, about the phase transitions taking place. For standard samples of vivianite, goethite, and maghemite, we compare the heating curves of the sample and a blank run, to identify

DTA-analogous information. In the case of goethite and vivianite, the reactions identified do not have a corresponding expression in susceptibility, demonstrating that this approach expands the utility of this common piece of equipment. We estimate the minimum enthalpy of reactions detectable and their mass dependence. Additionally, we show that this approach is successful in detecting the dehydration of vivianite in a mixed mineralogy natural sample.

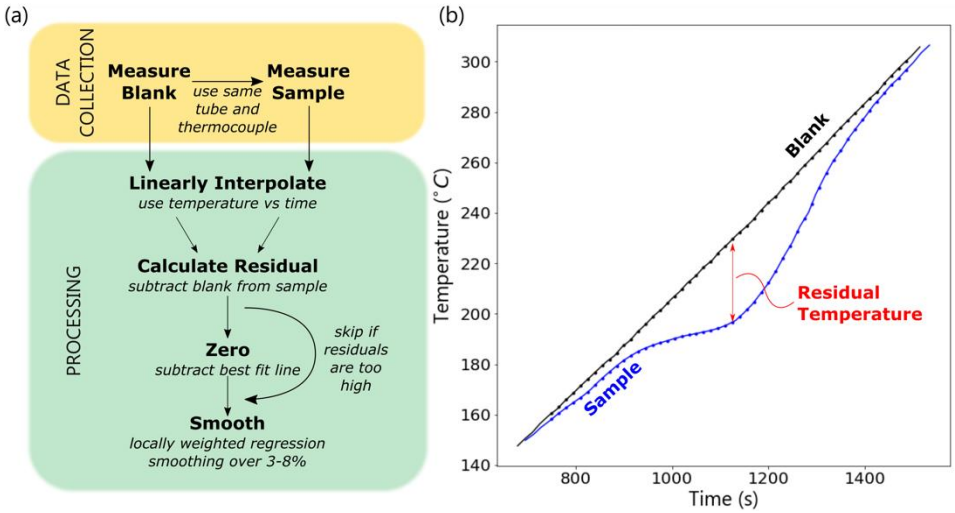

Figure 1. (a) Flow chart describing the procedure for data collection and processing (b) Excerpted data from vivianite heating curve showing the relationship between measured temperatures, interpolated points, and residual temperature during the endothermic dehydration reaction.

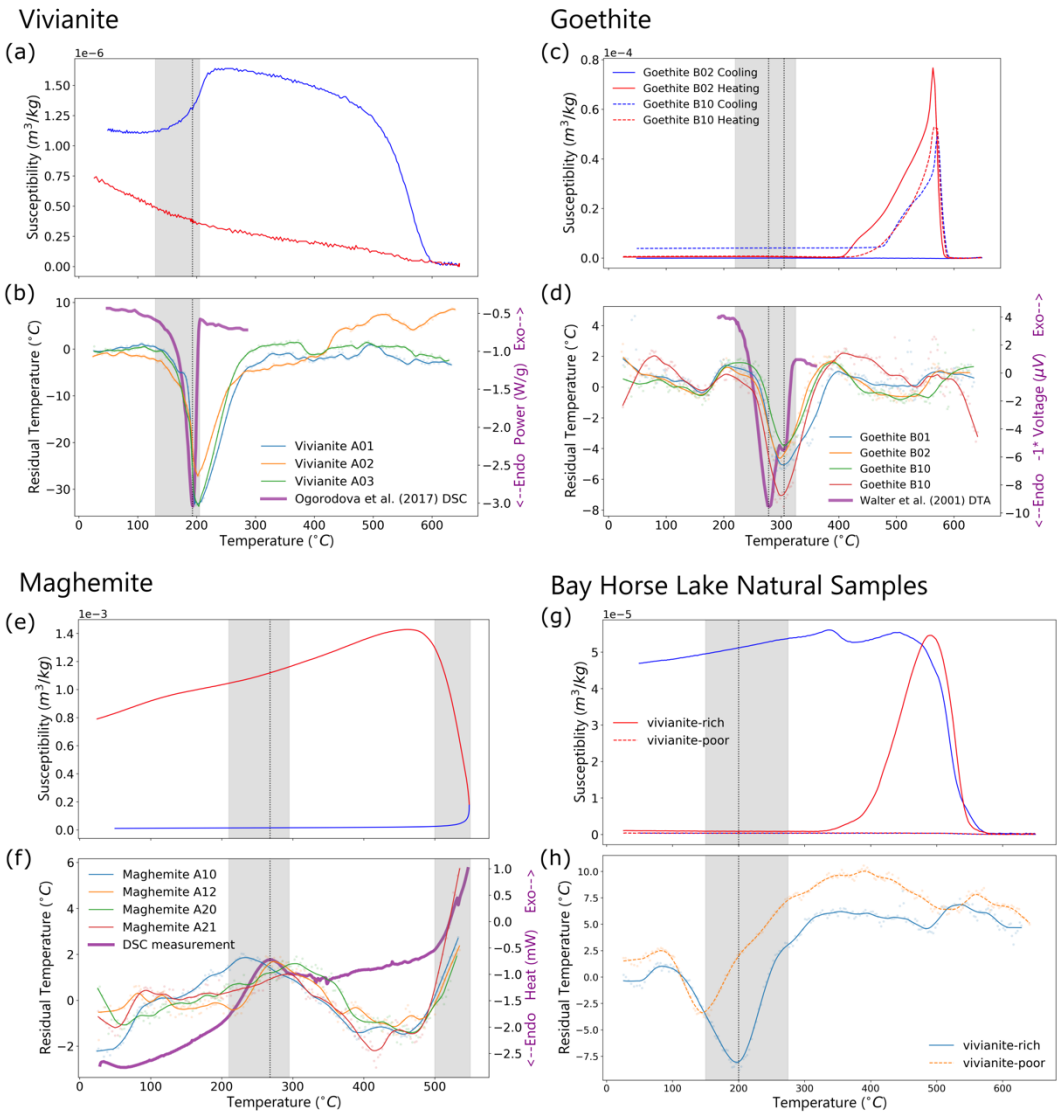

Figure 2. Graphs (a-f) show mineral standards measured on KLY-2 with the upper plot showing the low-field magnetic susceptibility during heating (red) and cooling (blue) and the lower plot showing the repeat heating rate analyses results and a comparative DSC/DTA plotted in purple. The extent of each reaction as detected by DSC/DTA is highlighted in grey with the peak temperature indicated by a dotted line. The standards include (a-b) Vivianite in which the heating rate analyses in (b) do not include detrending, (c-d) Goethite, and (e-f) maghemite. (g) Bay Horse Lake natural samples magnetic susceptibility and (h) heating rate analysis without detrending. The extent of the vivianite standards peaks is highlighted with the standard peak temperature indicated by a dotted line.

3. 通过碎屑锆石解析古代构造环境

翻译人：刘伟 inewway@163.com

Barham M, Kirkland C L, Handoko A D. ***Understanding ancient tectonic settings through detrital zircon analysis****[J]. Earth and Planetary Science Letters, 2022, 583: 117425.*

https://doi.org/10.1016/j.epsl.2022.117425

摘要：物源区的多样性和非均质性是决定沉积盆地碎屑锆石年龄分布的重要因素。活动会聚构造环境下的碎屑锆石样品以与弧/岩浆造山带相关的年轻年龄模式为主，而被动边缘和伸展环境下的碎屑锆石通常表现出分散的多模态年龄分布模式，反映出更广泛、地质各向异性更强的物源区和更强烈的沉积物循环过程。两个新定义的指标(i)与碎屑锆石年龄分布的第10百分位和第50百分位之间的时间差异，以及(ii)年龄群体形态和分散的修正分布分析，为区分地质活动背景（活动边缘和被动边缘盆地）提供了强有力的手段。重要的是，这种工具不需要沉积时代的约束。本文对这一“年龄分布指纹”在三个不同的新生代到元古代的案例研究中进行了评估，以证明该方法的构造分辨率和探索盆地演化过程的潜力。“年龄分布指纹”能够表征自俯冲相关板块构造开始以来的沉积路径历史和研究构造环境，即使在地层约束相对溃泛的地区。

ABSTRACT: The fertility and heterogeneity of source rocks play important roles in determining the age distribution of detrital zircon populations that accumulate in sedimentary basins. Detrital zircon samples in active convergent tectonic settings are typified by a dominance of well-defined young age modes associated with an arc/magmatic orogenic belt, while passive margins and extensional settings more commonly express dispersed polymodal age populations reflecting more extensive, geologically heterogeneous catchments and greater sediment recycling. Two newly defined metrics relating to (i) the temporal difference between the 10th and 50th percentiles of a detrital zircon age population, and (ii) a modified χ^2-distribution analysis of age population modality and dispersion, provide a powerful means of distinguishing between geologically active convergent systems and divergent/passive margin basins. Importantly, this tool does not require

knowledge of depositional age. This “age distribution fingerprint” is assessed in three distinct Cenozoic to Proterozoic case-studies to demonstrate the tectonic resolution of the approach and potential in refining views of basin evolution. The age distribution fingerprint offers the ability to characterize sediment routing histories and investigate tectonic settings since the onset of subduction related plate tectonics, even where stratigraphic constraints are lacking.

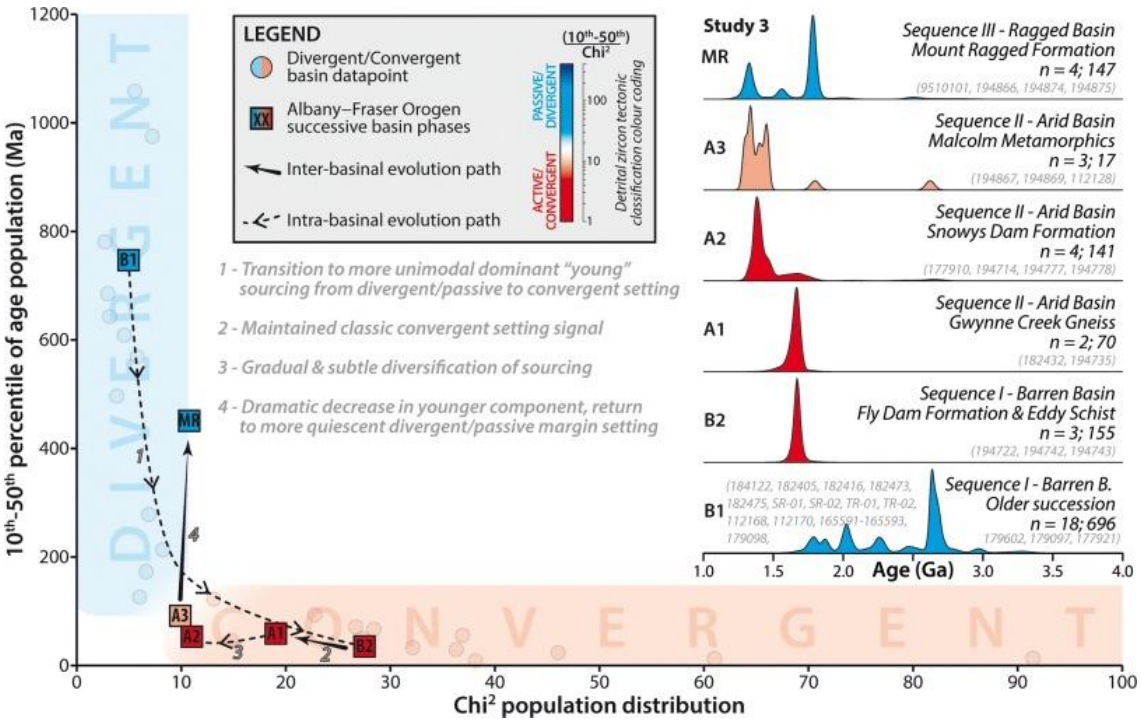

Figure 1. Bivariate discrimination plot of active convergent and divergent/passive margin tectonic settings applied to the Albany-Fraser Orogen case study. Sample symbols and kernel density estimate age spectra are color coded according to their combined detrital fingerprinting metric value in the legend. Greyscale italicized numbers represent sample numbers. Data sources - Clark et al. (2000), Spaggiari et al. (2015) and Waddell et al. (2015); n = number of samples; number of accepted analyses.

4. 东亚夏季风北部边缘地区在 H 和 D-O 事件期间的区域降雨反应

翻译人：杨会会 11849590@mail.sustech.edu.cn

Zhang S R, Xiao J L, Xu Q H, et al., ***Regional precipitation variations during Heinrich events and Dansgaard-Oeschger cycles in the northern margin of the East Asian summer monsoon region*** *[J]. Quaternary Sciences Reviews,2022,278,107380*

https://doi.org/10.1016/j.quascirev.2022.107380

摘要：由于缺乏长期、高分辨率的古气候记录，气候突变事件对东亚中高纬度地区区域气候变化的影响尚不清楚。我们提供了基于 AMS ^{14}C 定年的中国北方的呼伦湖，在过去 35ka 的详细孢粉记录。结果表明，区域植被在末次冰期发生了 4 次变化，主要表现为耐寒、耐旱植物增多，植被覆盖减少。这些事件与起源于北大西洋地区的 Heinrich 事件(H3、H2 和 H1)和新仙女木事件(YD)同时发生。此外，在温暖的 Dansgaard-Oeschger(D-O)旋回和 Bøling- allerød (B/A)间冰阶时期的记录表明，呼伦湖附近山地阔叶落叶林扩张，而呼伦湖附近的典型草原植被扩张。总体而言，呼伦湖地区在气候突变事件期间的区域植被变化结构和幅度与格陵兰冰芯氧同位素记录不同；然而，它们与东亚同时期石笋氧同位素记录相似。因此，在 H 事件和 D-O 旋回期间，呼伦湖地区的降水主要受东亚夏季风(EASM)强度变化的控制而增加或减少。我们的研究结果表明，东亚夏季风的变化与北大西洋气候系统在百年至千年尺度上存在物理联系。此外，区域降水变化幅度在末次冰期和末次冰盛期的 H 事件和 D-O 旋回期间较低；但是，区域降水的变幅在末次冰消期的 H1 事件和 B/A 变暖事件期间显著增大。我们认为，NHSI 和陆面条件(冰盖和海平面)的差异是导致东亚夏季降水在不同时段对这些突变气候事件响应差异的原因。

ABSTRACT: Due to the scarcity of long, high-resolution paleoclimate records, the effects of abrupt climatic events on regional climate variations in middle to high latitudes of East Asia are unclear. We present a detailed pollen record for the past 35,000 years, with an AMS ^{14}C chronology, from Hulun Lake in northern China. The results reveal four episodes of regional vegetation change during the Last Glaciation, characterized by increases in cold-resistant and drought-tolerant plants and

decreased regional vegetation cover. These episodes coincided with Heinrich events (H3, H2 and H1) and the Younger Dryas event (YD) that originated in the North Atlantic region. Additionally, during the warm intervals of the Dansgaard-Oeschger (D-O) cycles and the Bølling-Allerød (B/A) interstadial recorded in Greenland ice cores, patches of broadleaved deciduous forest expanded in the surrounding mountains while typical steppe vegetation expanded in the vicinity of Hulun Lake. Overall, the structure and amplitude of regional vegetation change in the Hulun Lake region during abrupt climatic events differ from the registration of these events in the oxygen isotope records from Greenland ice cores; however, they are similar to coeval stalagmite oxygen isotope records from East Asia. Thus, we suggest that the regional climate variations were characterized by increased or decreased precipitation during H events and D-O cycles in the Hulun Lake region, which was mainly controlled by changes in the intensity of the East Asian summer monsoon (EASM). Our results suggest that the variability of the EASM was physically linked to the North Atlantic climate system on centennial- to millennial-scale. In addition, the amplitude of regional precipitation variations during H events and D-O cycles was low during the interstadial of the Last Glaciation and the Last Glacial Maximum; however, the amplitude of regional precipitation variations during H1 event and B/A warming event was substantially greater during the Last Deglaciation. We suggest that differences in NHSI and land surface conditions (ice sheets and sea level) were responsible for the contrasting responses of EASM precipitation to these abrupt climatic events during different intervals.

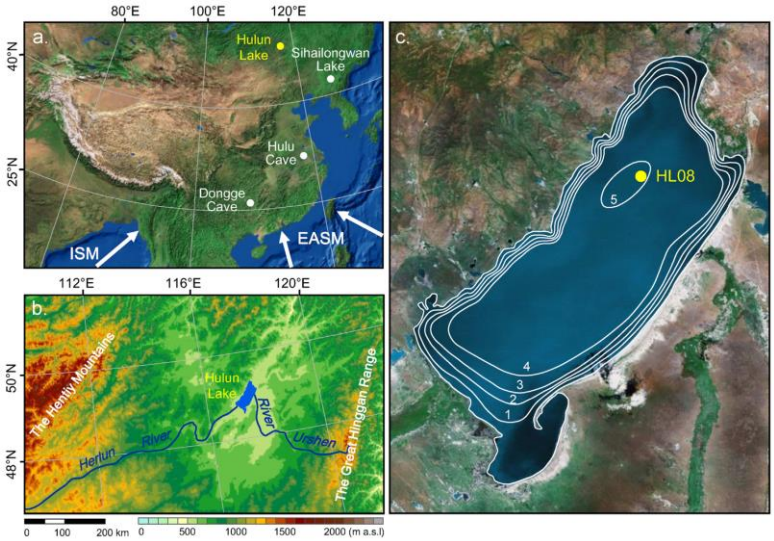

Figure 1. (a) Map of East Asia showing the location of Hulun Lake and the sites mentioned in the text, and the modern trajectories of the East Asia summer monsoon (EASM) and the Indian summer onsoon (ISM). (b) Topographic map of the Hulun Lake region. (c) Satellite image of Hulun Lake showing the location of core HL08. The bathymetric survey of the lake was conducted in July 2005 (contours in m) (the satellite image is from https://www.arcgis.com).

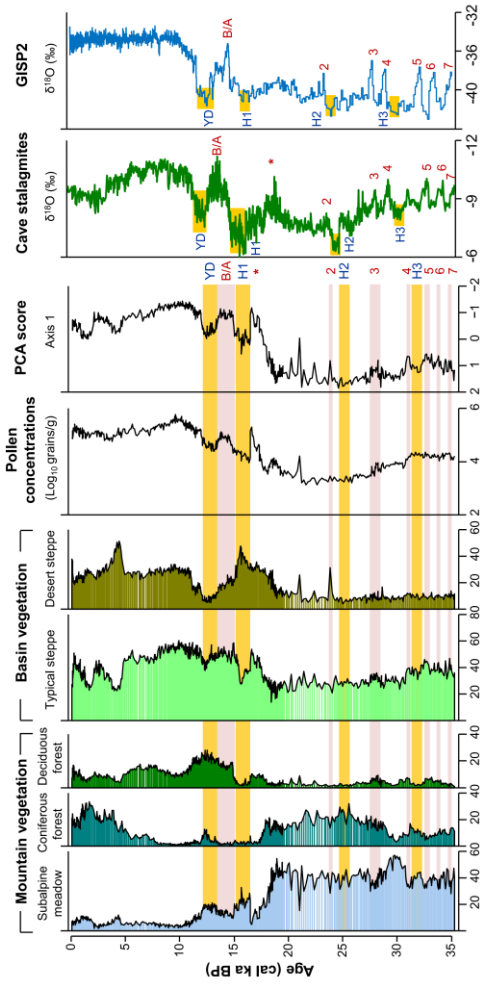

Figure 2. Variation of pollen ecological groups, pollen concentrations and PCA axis-1 sample scores for core HL08 during the past 35,000 cal yr BP. H events and D-O cycles are indicated by yellow and red shading, respectively, which are based on a comparison with the GISP2 Greenland ice core oxygen isotope record (Stuiver and Grootes, 2000) and composite Chinese speleothem oxygen isotope records (Cheng et al., 2016). "*" indicates an exceptionally strengthened East Asian summer monsoon event recorded in the speleothem oxygen isotope record from Hulu cave (Wu et al., 2009). (For interpretation of the references to color in this figure legend, the reader is referred to the Web version of this article.)

5. Evron Quarry (1.0-0.8 Mya)早期用火的潜在特征

翻译人：曹伟 11930854@qq.com

Stepka Z, Azuri I, Horwitz L, et al. ***Hidden signatures of early fire at Evron Quarry (1.0 to 0.8 Mya)*** *[J]. PNAS, 2022, 119(25):e2123439119.*

https://doi.org/10.1073/pnas.2123439119

摘要：用火技术是古人类进化的关键因素。早期古人类遗址用火的识别主要依赖于对文物物理变化的初步视觉评估，这可能会低估考古记录中用火的普遍程度。本研究中，我们使用了一系列光谱技术来弥补视觉特征在用火记录中的缺失，并证明了 Evron Quarry（以色列）旧石器时代（LP）早期露天遗址中存在烧过的动物和岩屑残存，年代介于 1.0 至 0.8 Mya 之间，大致与 Gesher Benot Ya'aqov 同期，那里记录了早期的用火技术。我们建议重新研究缺乏用火技术视觉线索的其他旧石器时代遗址的发现，以对早期人类行为和用火之间关系的起源、演化和时空分布提供新的视角。

ABSTRACT: Pyrotechnology is a key element of hominin evolution. The identification of fire in early hominin sites relies primarily on an initial visual assessment of artifacts physical alterations, resulting in potential underestimation of the prevalence of fire in the archaeological record. Here, we used a suite of spectroscopic techniques to counter the absence of visual signatures for fire and demonstrate the presence of burnt fauna and lithics at the Lower Paleolithic (LP) open-air site of Evron Quarry (Israel), dated between 1.0 and 0.8 Mya and roughly contemporaneous to Gesher Benot Ya’aqov where early pyrotechnology has been documented. We propose reexamining finds from other LP sites lacking visual clues of pyrotechnology to yield a renewed perspective on the origin, evolution, and spatiotemporal dispersal of the relationship between early hominin behavior and fire use.

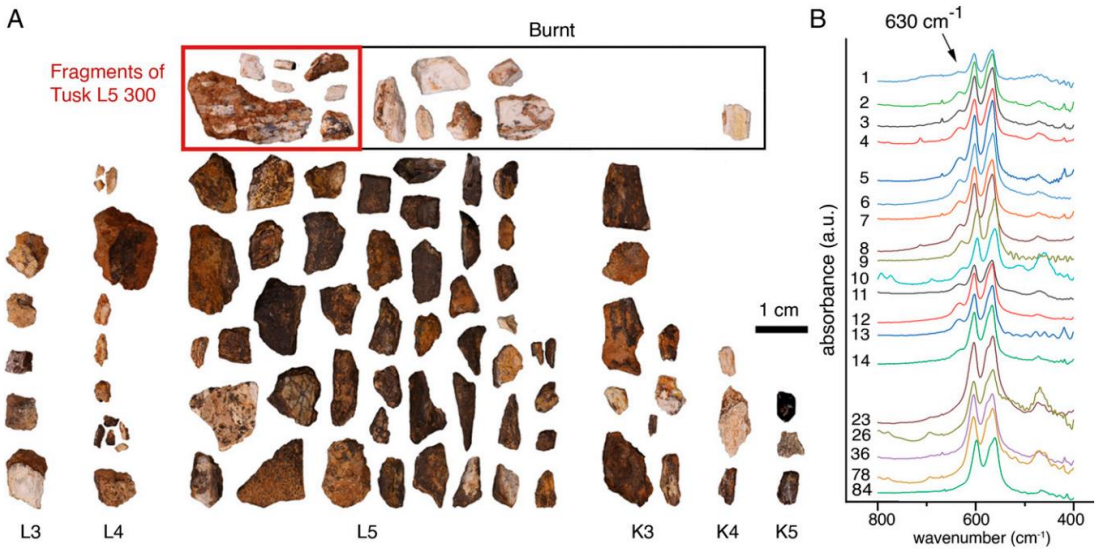

Figure 1. Faunal assemblage. (A) Photographic visualization of the whole analyzed faunal assemblage divided by excavation squares labeled as L3, L4, L5, K3, K4, and K5 at the Bottom. (B) FTIR spectra of all analyzed faunal remains in the spectral region between 800 and 400 cm^{-1}.

6. 南非沙尘在间冰期对高纬度和东南极洲的贡献

翻译人：王敦繁 Dunfan-w@foxmail.com

Gili, S., Vanderstraeten, A., Chaput, A. et al. ***South African dust contribution to the high southern latitudes and East Antarctica during interglacial stages [J]***. *Commun Earth Environ* 3, 129 (2022). https://doi.org/10.1038/s43247-022-00464-z

摘要：风尘是大气成分和气候变化的天然示踪剂。然而，关于南半球的粉尘循环仍有很多需要了解的地方。人们已作出重大努力，试图解开向南大洋和东南极洲输送粉尘的潜在源区之谜。本文提出了风尘源区的综合地球化学特征，其作为高纬度环境的粉尘供应者的作用被严重低估。对非洲南部纳米比亚沿海主要产尘地区(Kuiseb、Omaruru 和 Huab 河流域以及纳米布沙海地区)收集的沉积物进行了放射性同位素比率和稀土元素分析。我们发现，在温暖时期，非洲南部的沙尘特征可以在南半球的记录中找到，特别是在南大洋的大西洋部分和东南极高原的外围地区。

ABSTRACT: Mineral dust is a natural tracer of atmospheric composition and climate variability. Yet, there is still much to be known about the Southern Hemisphere dust cycle. Major efforts have attempted to solve the puzzle of the origin of the potential source areas contributing dust to the Southern Ocean and East Antarctica. Here we present a comprehensive geochemical characterization of a source area, whose role as a dust supplier to high latitude environments has significantly been underestimated. Sediments collected within the major dust-producing areas along the Namibian coast in Southern Africa (Kuiseb, Omaruru and Huab river catchments and the Namib Sand Sea region), were analyzed for radiogenic isotope ratios and rare earth element concentrations. We find that during warm periods, the Southern African dust signature can be found in archives of the Southern Hemisphere, especially in the Atlantic sector of the Southern Ocean and peripheral areas of the East Antarctic plateau.

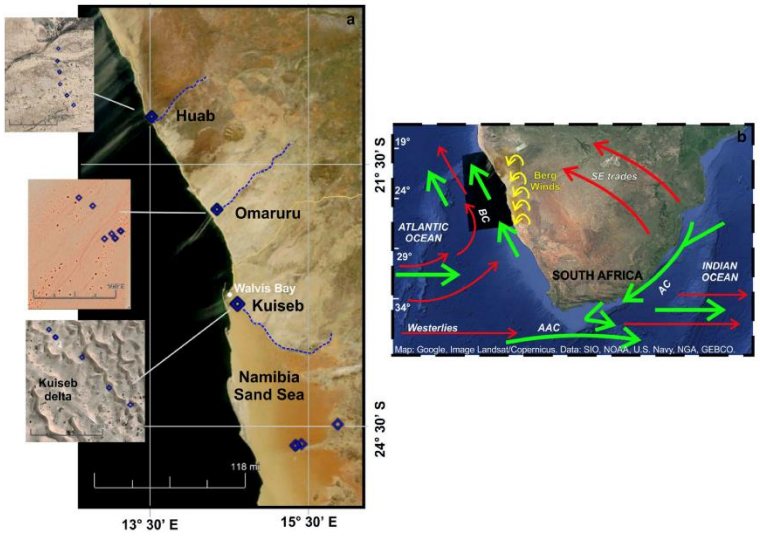

Figure 1. Geographical and climatological characterization of Southern Africa Potential dust source areas. a satellite image of dust plumes originated off the coast of Namibia captured in May 2013 by The Moderate Resolution Imaging Spectroradiometer (MODIS) on NASA's Terra satellite showing the study areas of Huab, Omaruru, Kuiseb and the Nambia Sea Sand. The hydrographic Huab, Omaruru and Kuiseb systems are indicated by the blue lines. b map of southwestern Africa showing the major features of the regional climate system. Main oceanic currents are indicated in bold green arrows and atmospheric circulations in red (south easterly trade and westerlies winds) and yellow (Berg winds). BC: Benguela Current; ACC: Antarctic Circumpolar Current; AC: Aghulas Current. The map in Fig. b was built using Google Earth Pro, Image Landsat/Copernicus; Data: SIO, NOAA, U.S Navy, NGA, GEBCO, 13 December 2015.

7. 利用地磁场古强度确定鹤庆盆地晚更新世湖相沉积物年代学及其古气候意义

翻译人：王浩森 11930841@mail.sustech.edu.cn

Xu X, Qiang X, Li X, et al. ***Determination of the optimized late Pleistocene chronology of a lacustrine sedimentary core from the Heqing Basin by geomagnetic paleointensity and its paleoclimate significance****[J]. Catena, 2022, 212: 106095.*

https://doi.org/10.1016/j.catena.2022.106095

摘要：中国西南部长且连续的湖泊沉积序列真实地记录了印度夏季风（ISM）的演化。然而，^{14}C 测年的有限测年范围（<50 ka）限制了对末次冰期旋回的高分辨率研究。为了优化其 AMS ^{14}C 年代学，我们从鹤庆盆地的湖相沉积岩芯中得到了相对古强度（RPI）记录。岩石磁性分析表明，SD 和涡流态磁铁矿（和/或磁赤铁矿）是湖泊沉积物的主要磁性矿物。浓度依赖（SIRM，ARM）和粒度依赖（ARM/SIRM）参数的变化符合 RPI 研究的标准。因此，我们通过 $NRM_{20\text{-}40\,mT}/SIRM_{20\text{-}40\,mT}$ 确定了 RPI，其中 $NRM_{20\text{-}40\,mT}$ 表示 20-40 mT 之间退磁的 NRM。使用 40 ka BP 以来的 6 个 AMS ^{14}C 年龄作为约束条件，通过将 RPI 记录中的低值与目标古强度叠加 PISO-1500 的低值相关联，确定了 7 个年龄控制点。基于 7 个 RPI 年龄控制点和气候转换末期 II，我们通过二项拟合建立了 HQ 钻芯上部 11.1 m 的可靠年代学框架。我们的 RPI 曲线和全球其他目标古强度曲线的一致变化表明年代学结果是可靠的。在我们优化的年表中，ARM/SIRM 中明显的进动周期表明，ISM 是对末次冰期周期中太阳辐射的直接反应。MIS 3 期间，梅西针叶树和热带亚热带树木的高含量所表明的强 ISM 转移到 MIS 5a。因此，主要由 ^{14}C 年龄模型推断的中国“MIS 3 巨型古湖”假说受到了挑战。

ABSTRACT: Long and continuous lacustrine sedimentary sequences from SW China faithfully recorded the evolution of the Indian summer monsoon (ISM). However, the limited dating range (<50 ka) of ^{14}C dating has restricted high-resolution research on the last glacial cycle.

We presented a relative paleointensity (RPI) record from a lacustrine sedimentary core from the Heqing Basin to optimize its AMS ^{14}C chronology. Detailed rock magnetic analyses indicated that SD and vortex state magnetite (and/or maghemite) was the dominant magnetic mineral of lacustrine

sediments. Moderate variations in concentration-dependent (SIRM, ARM) and grain-size-dependent (ARM/SIRM) parameters satisfied the criteria for the RPI studies. Consequently, we determined the RPI by $NRM_{20\text{-}40\ mT}/SIRM_{20\text{-}40\ mT}$, where $NRM_{20\text{-}40\ mT}$ denotes the NRM after demagnetization between 20 and 40 mT. Using 6 AMS 14C dates younger than 40 ka BP as constraints, 7 age control points were determined by correlating the lows in the RPI record with those of the target paleointensity stacks PISO-1500. We established a reliable chronological framework of the upper 11.1 m of the HQ drill core by binomial fitting based on the 7 RPI age control points and the climatic transition termination II. The consistent variations in our RPI curve and other global target paleointensity curves indicated that the optimized chronology was reliable.

In our optimized chronology, the visible precession cycle in ARM/SIRM indicated that the ISM was a direct response to solar insolation during the last glacial cycle. The strong ISM suggested by the high content of Mesic conifers and tropical and subtropical trees during MIS 3 shifted to MIS 5a. Thus, the "MIS 3 Mega-paleolake" hypothesis in China, which was mainly deduced by the ^{14}C age model, was challenged.

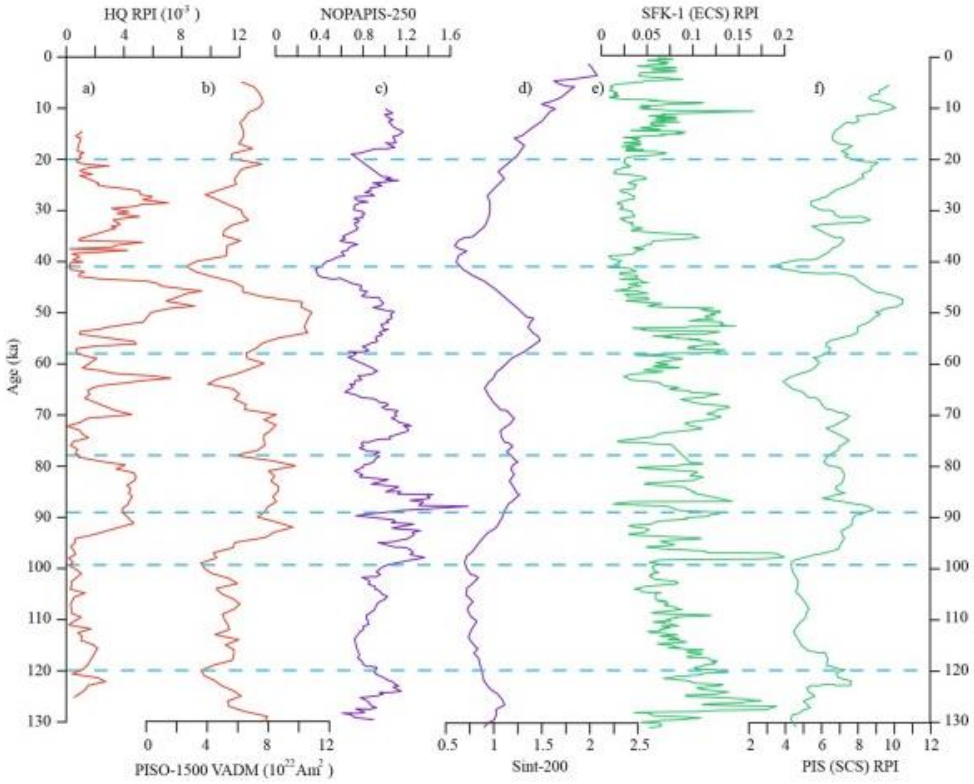

Figure 1. Correlation of the PRI record from the HQ drill core with global target RPI stacks. a) PRI record from the HQ drill core; b) PISO-1500; c) NOPAPIS-250; d) Sint-200; e) SFK-1 (ECS); f) PIS (SCS). The dashed blue lines indicate the consistent tie points.

8. 月球缺少长期的古磁场

翻译人：张伟杰 12031188@mail.sustech.edu.cn

Tarduno J A, Cottrell R D, Lawrence K, et al. ***Absence of a long-lived lunar paleomagnetosphere****[J]. Science Advances, 2021, 7(32): eabi7647.*

https://doi.org/10.1126/sciadv.abi7647

摘要：确定过去存在或缺失长期的月球磁场对了解月球内部和表面如何演变至关重要。在这里，我们展示了与 200 万年前陨石坑有关的撞击玻璃记录的类似地球的较强磁场，这为撞击可以给月球或其他行星样品施加较强磁场信号提供了证据。此外，我们的研究表明，阿波罗样品中含有约 39、36、33 和 32 亿年前形成能够记录较强核心发电机磁场的磁性硅酸盐包裹体，但其没有记录到磁性。综上所述，这些数据表明月球没有寿命很长的核心发电机。因此，月球没有受到持续古磁层的保护，月球风化层应该埋藏着过去 40 亿年从太阳风和地球磁层中获得的 ^{3}He、水和其他挥发性资源。

ABSTRACT: Determining the presence or absence of a past long-lived lunar magnetic field is crucial for understanding how the Moon's interior and surface evolved. Here, we show that Apollo impact glass associated with a young 2 million–year–old crater records a strong Earth-like magnetization, providing evidence that impacts can impart intense signals to samples recovered from the Moon and other planetary bodies. Moreover, we show that silicate crystals bearing magnetic inclusions from Apollo samples formed at ~3.9, 3.6, 3.3, and 3.2 billion years ago are capable of recording strong core dynamo–like fields but do not. Together, these data indicate that the Moon did not have a long-lived core dynamo. As a result, the Moon was not sheltered by a sustained paleomagnetosphere, and the lunar regolith should hold buried ^{3}He, water, and other volatile resources acquired from solar winds and Earth's magnetosphere over some 4 billion years.

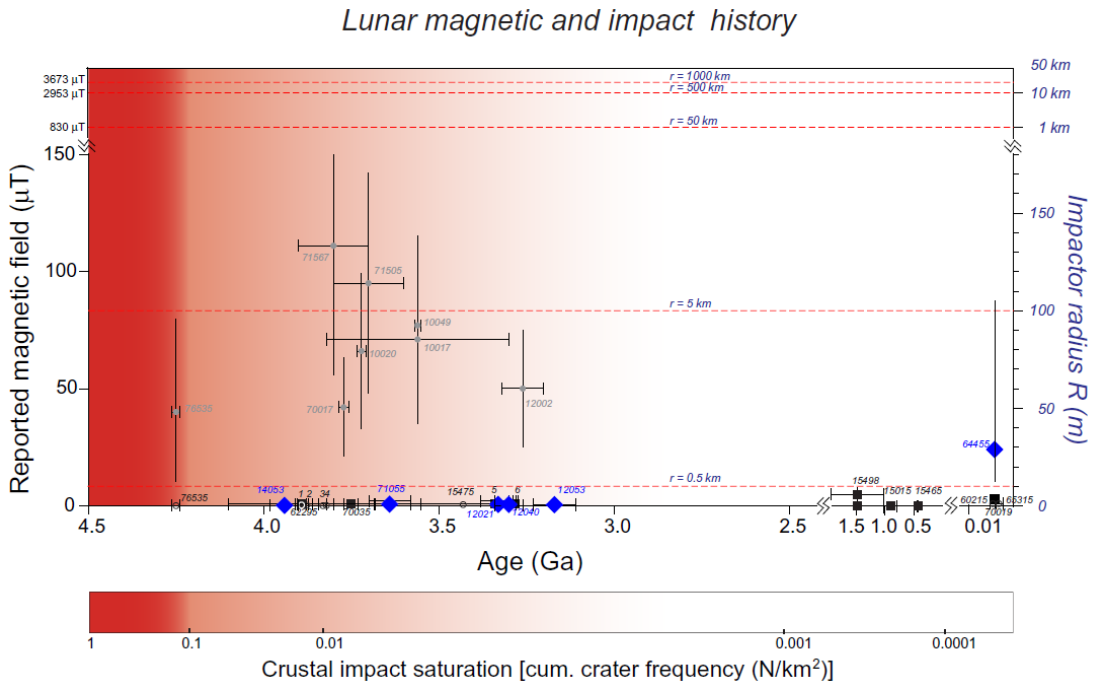

Figure 1. Lunar magnetic and impact history. Reported field strength measurements from select Apollo samples (table S5) shown as follows: gray filled circles, nonthermal methods; open circles, no evidence for primary remanence, interpreted as magnetic contamination or results of magnetic interactions/phase changes during analysis; black squares, data based on thermal analyses. All sample numbers are listed except the following: 1, 68815 (open circle); 2, 62235; 3, 72215; 4, 75055; 5, 60015 (black square); and 6, 15016. Blue diamonds, thermal analysis values (this work). The right axis shows field impactor radius (R) capable of generating the field intensities by magnetizations induced by charge separation. Radius (r) values shown by dashed lines are field values at r = 50R. The shaded region reflects the degree of crustal impact saturation (see Materials and Methods).

9. 加拿大北极群岛对 Scandinavia 冰盖扩张的重要性

翻译人：李海 12031330@mail.sustech.edu.cn

Lofverstrom M, Thompson D M, Otto-Bliesner B L, et al. ***The importance of Canadian Arctic Archipelago gateways for glacial expansion in Scandinavia*** *[J]. Nature Geoscience, 2022. https://doi.org/10.1038/s41561-022-00956-9*

摘要：末次冰期开始于距今约 11.6 万年前北半球的夏季太阳辐射较低的时期。在北美进入冰期之后，海洋沉积物记录了高纬翻转环流的减弱以及横跨北大西洋盆地千年尺度上冰川的东进。模型研究表明，减少的太阳辐射可以在北美和西伯利亚开始；然而，靠近温带北大西洋通常会限制 Scandinavia 半岛冰层的生长。利用一个耦合的地球系统-冰盖模型，作者认为，北美冰川的形成有助于 Scandinavia 半岛的冰川扩张。随着大型连贯的浮冰形成并开始充填加拿大群岛的海洋通道，北太平洋和北极的水通过群岛转移到格陵兰岛的东部，导致北大西洋深层对流区域盐度降低、海冰扩张和降温，这足以引发 Scandinavia 半岛进入冰期。这一机制也可能有助于解释新仙女木时期的寒冷逆转和 Scandinavia 冰盖在末次冰期的几次温暖事件后快速扩张。

ABSTRACT: The last glacial cycle began around 116,000 years before present during a period with low incoming solar radiation in Northern Hemisphere summer. Following the glacial inception in North America, the marine sediment record depicts a weakening of the high-latitude ocean overturning circulation and a multi-millennial eastward progression of glaciation across the North Atlantic basin. Modelling studies have shown that reduced solar radiation can initiate inception in North America and Siberia; however, the proximity to the temperate North Atlantic typically precludes ice growth in Scandinavia. Using a coupled Earth-system-ice-sheet model, we show that ice forming in North America may help facilitate glacial expansion in Scandinavia. As large coherent ice masses form and start filling the ocean gateways in the Canadian Archipelago, the transport of comparatively fresh North Pacific and Arctic water through the archipelago is diverted east of Greenland, resulting in a freshening of North Atlantic deep convection regions, sea-ice expansion and a substantial cooling that is sufficient to trigger glacial inception in Scandinavia. This

mechanism may also help explain the Younger Dryas cold reversal and the rapid regrowth of the Scandinavian Ice Sheet following several warm events in the last glacial period.

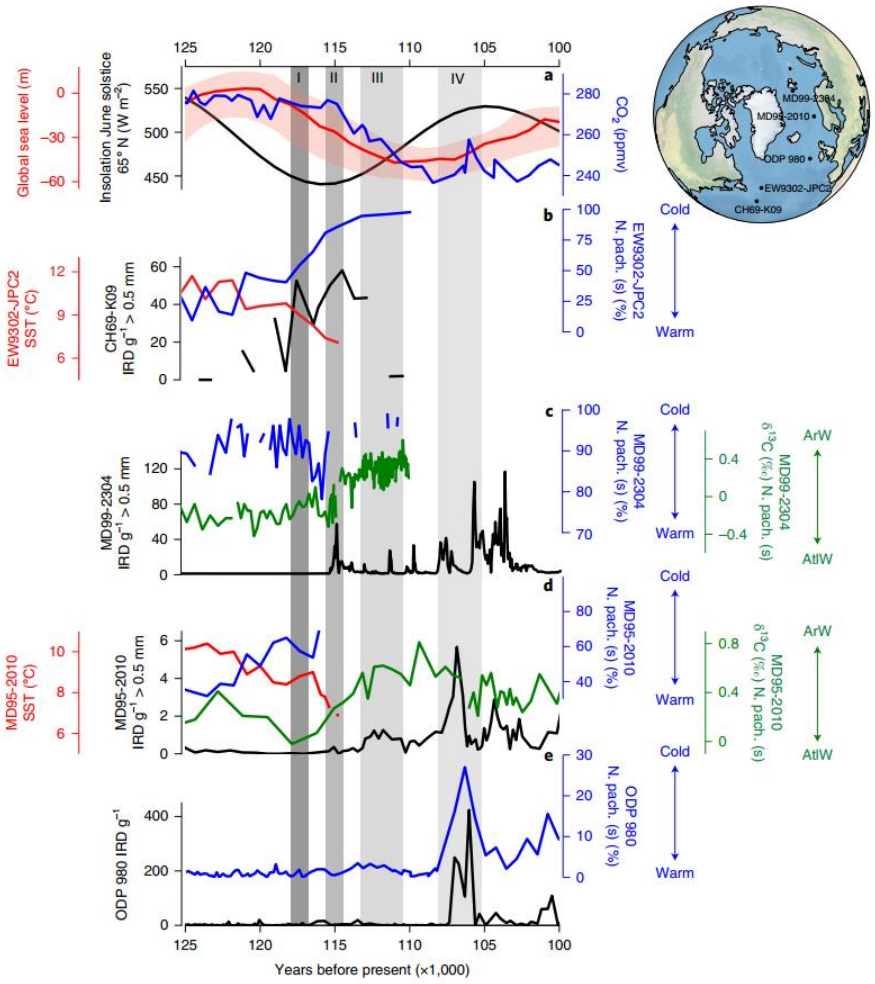

Figure 1. a, Global sea-level change[3], top-of-atmosphere insolation at 65° N at June solstice1 and CO_2 concentration[51]. b–e, Data from North Atlantic sediment cores. Coloured lines in b–e depict SST (red), IRD (black), abundance of Neogloboquadrina pachyderma sinistral (N. pach. (s); blue), a planktonic foraminifera indicator species for polar waters and its $\delta^{13}C$ variations ($\delta^{13}C$ N. pach. (s); green). Positive/negative $\delta^{13}C$ N. pach. (s) indicates dominance of Arctic water (ArW)/Atlantic water (AtlW), respectively. Panels depict data from the western (cores CH69-K09 and EW9302-JPC2; ref. [6]) (b), northeastern (core MD99-2304; refs. [6,7,8]) (c), eastern (core MD95-2010; refs. [7,8]) (d) and east-central (core ODP 980; refs. [6,10]) (e) North Atlantic, respectively. Proxy-data sites are indicated in the top right corner. Discontinuous lines in b–d are due to missing data in the proxy datasets. Maps generated using Cartopy with Natural Earth shapefiles.

10. 威德尔海深水碳封存作用将会在 2100 年突然减弱

翻译人：张亚南 zhangyn3@mail.sustech.edu.cn

Nissen C, Timmermann R, Hoppema M, et al. ***Abruptly attenuated carbon sequestration with Weddell Sea dense waters by 2100*** *[J]. Nature Communications, 2022, 13, 3402.*

https://doi.org/10.1038/s41467-022-30671-3

摘要：南极底层水的形成，在百年尺度上是一个有效的碳封存载体，如威德尔海。到目前为止，在不断变化的环境条件下，碳封存的可能变化迄今为止尚未得到量化，这主要是由于模拟高纬度大陆架相关过程存在困难。文中，作者使用包括冰盖空洞和海洋碳循环的模型设置，揭示了到 2100 年，在高排放背景下，威德尔海南部的深海碳积累速度突然减弱，仅为 1990 年的 40%，而在 2050s 和 2080s 这一速度比 1990s 分别高 2.5 倍和 4 倍。通过评估深海碳平衡和水质量转换，作者将这种下降归因于南部威德尔海大陆架上温暖深水的增加，海冰形成减少 16%，冰架基底融化增加了 79%。总之，这些变化降低了新形成的底层水的密度和体积，减少了与之相关的深海碳输送。

ABSTRACT: Antarctic Bottom Water formation, such as in the Weddell Sea, is an efficient vector for carbon sequestration on time scales of centuries. Possible changes in carbon sequestration under changing environmental conditions are unquantified to date, mainly due to difficulties in simulating the relevant processes on high-latitude continental shelves. Here, we use a model setup including both ice-shelf cavities and oceanic carbon cycling and demonstrate that by 2100, deep-ocean carbon accumulation in the southern Weddell Sea is abruptly attenuated to only 40% of the 1990s rate in a high-emission scenario, while the rate in the 2050s and 2080s is still 2.5-fold and 4-fold higher, respectively, than in the 1990s. Assessing deep-ocean carbon budgets and water mass transformations, we attribute this decline to an increased presence of modified Warm Deep Water on the southern Weddell Sea continental shelf, a 16% reduction in sea-ice formation, and a 79% increase in ice-shelf basal melt. Altogether, these changes lower the density and volume of newly formed bottom waters and reduce the associated carbon transport to the abyss.

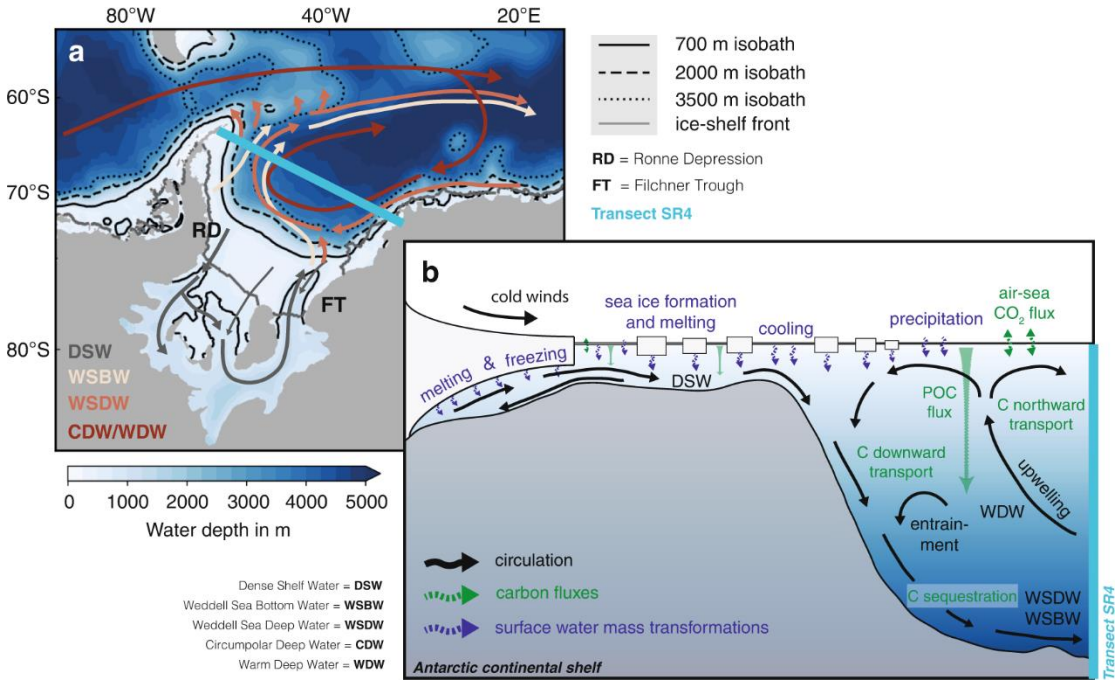

Figure 1. Sketch illustrating the major processes involved. a Water depth in m below the ocean surface in the Weddell Sea and a schematic view of the general two-dimensional circulation in the area. The transect SR4 of the World Ocean Circulation Experiment is marked in mint, and different water masses are distinguished by colors. b Typical section from the Antarctic continent to the transect SR4, with general features of the overturning circulation sketched in black. Highlighted in blue are surface water mass transformations by buoyancy fluxes, and carbon fluxes are marked in green. CDW Circumpolar Deep Water, WDW Warm Deep Water, WSDW Weddell Sea Deep Water, WSBW Weddell Sea Bottom Water, DSW Dense Shelf Water, POC particulate organic carbon.

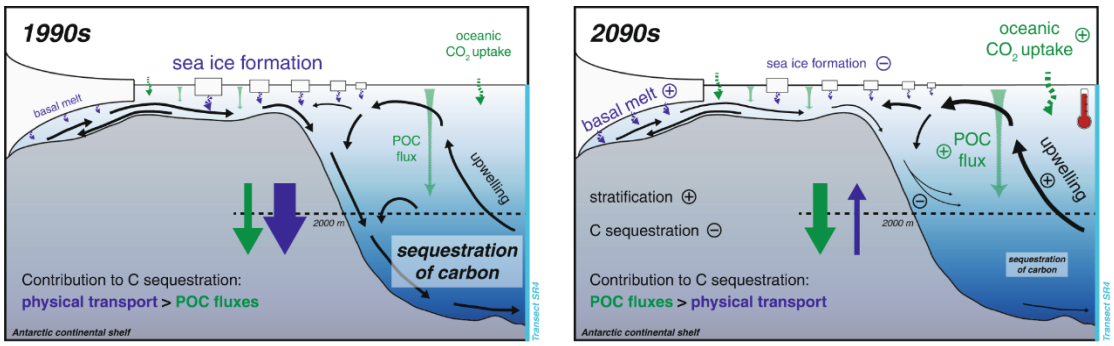

Figure 2. Sketch illustrating the simulated changes over the 21st century in the high-emission scenario. Compared to the 1990s, deep-ocean carbon sequestration in the southern Weddell Sea is

reduced by 60%, which is largely attributed to a reduction in the physical transport of carbon to the abyss. In particular, sea-ice formation is reduced by 16%, and ice-shelf basal melt increases by 79%, which both act to decrease the density of water on the continental shelf. Despite the 10-fold increase in oceanic CO_2 uptake and a 47% increase in sinking fluxes of biotic particles (POC), the decline in physically-driven downward transport dominates, as newly formed lighter dense waters on the continental shelf are transferred to shallower depths in the 2090s, reducing carbon accumulation in the deep ocean. In the sketch, font sizes and arrow thicknesses in the 2090s are scaled to approximately represent the magnitude of the simulated processes or fluxes.

11. 全球降温引发了密西西比纪中晚期的生物多样性危机

翻译人：刘宇星 11811211@mail.sustech.edu.cn

Yao L, Jiang G, Mii H, et al. ***Global cooling initiated the Middle-Late Mississippian biodiversity crisis****[J]. Global and Planetary Change, 2022: 103852.*

https://doi.org/10.1016/j.gloplacha.2022.103852

摘要：在密西西比纪，多细胞礁类和其他海洋动物群逐渐从泥盆纪晚期大灭绝中恢复过来，并在 Visean 晚期(~334-332Ma)达到顶峰。动物群多样性从 Visean (~332-330Ma)到 Serpukhovian (~330-323Ma) 开始下降，具有显著的属/物种损失和生态系统重建特征。这场密西西比纪中晚期生物多样性危机(M-LMBC)被认为是由与晚古生代冰河时代(LPIA)相关的全球变冷事件引起，但现有的沉积学和温度代理数据表明，标志着全球变冷事件开始的主要冰期发生在约 332Ma 的初始生物多样性下降约 4 Myr 之前或约 1-5 Myr 之后。这里，我们报告了晚 Visean-Serpukhovian 期（或称密西西比级中晚期；~334-323Ma）华南地层的成岩筛选后且保存完好的腕足类方解石($\delta^{18}O_{calcite}$)的氧同位素数据。 $\delta^{18}O_{calcite}$ 数据显示从-4.6±0.2‰到-2.7±0.5‰的约 2.0‰正偏移，估计在 Visean 晚期约 332.5-331.5Ma 期间海面温度(SST)下降约 4.7-5.5˚C。这一降温事件恰好对应多细胞礁类丰度迅速下降事件，随后底栖动物多样性下降。$\delta^{18}O_{calcite}$ 数据与校准的沉积学和生物多样性数据相结合，证明了 LPIA 主要冰川期内晚 Visean (~332Ma)与 M-LMBC 的开始之间具有耦合性。

ABSTRACT: During the Mississippian period, metazoan reefs and other marine faunas gradually recovered from the Late Devonian mass extinctions and reached a peak in the late Visean (~334–332Ma). Faunal diversity started to decline from the latest Visean (~332–330Ma) through Serpukhovian (~330–323Ma), with significant genera/species losses and ecosystem reconstruction. This Middle-Late Mississippian biodiversity crisis (M-LMBC) was thought to have been caused by global cooling associated with the late Paleozoic Ice Age (LPIA), but existing sedimentological and temperature proxy data suggest that the global cooling event—that marks the onset of the main glaciation phase of LPIA—happened either ~4 Myr before or ~ 1–5Myr after the initial biodiversity

decline at ~332Ma. Here, we report oxygen isotope data of diagenetically screened, well-preserved brachiopod calcite ($\delta^{18}O_{calcite}$) from late Visean-Serpukhovian (or Middle-Late Mississippian; ~334–323Ma) strata in South China where biodiversity data are well documented. The $\delta^{18}O_{calcite}$ data reveal a ~2.0‰ positive shift from −4.6 ± 0.2‰ to −2.7 ± 0.5‰ with an estimated ~4.7–5.5°C drop in sea surface temperature (SST) during ~332.5–331.5Ma in the late Visean. This cooling event coincides with fast decline of metazoan reef abundance, followed by decrease of benthic faunal diversity. The $\delta^{18}O_{calcite}$ data, in combination with calibrated sedimentological and biodiversity data, demonstrate the coupling between late Visean (~332Ma) onset of the main glaciation phase of the LPIA and initiation of the M-LMBC.

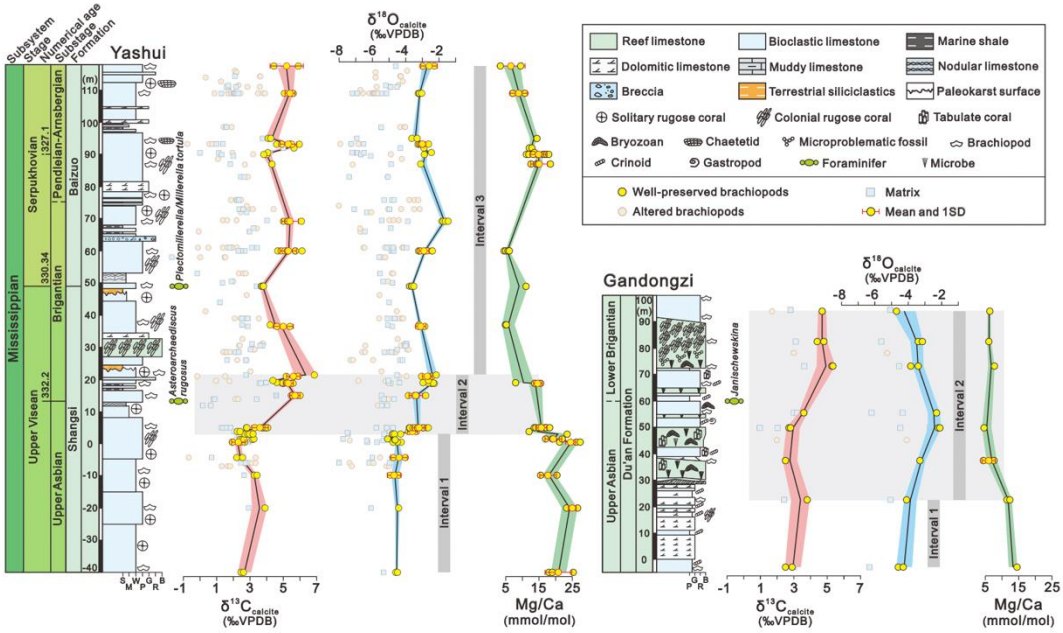

Figure 1. Late Visean-Serpukhovian $\delta^{13}C_{calcite}$, $\delta^{18}O_{calcite}$, and Mg/Ca variations of well-preserved brachiopods (yellow circle) from the Yashui and Gandongzi sections in South China. The solid line and shaded area in each panel represent the LOWESS cure and variation range (±1σ), respectively. For comparison, isotope data of altered brachiopods and limestone matrix are also plotted but they are not used to construct the temporal isotope curves. B: Boundstone; R: Rudstone; G: Grainstone; P: Packstone; W: Wackestone; M: Mudstone; S: Shale. (For interpretation of the references to color in this figure legend, the reader is referred to the web version of this article.)

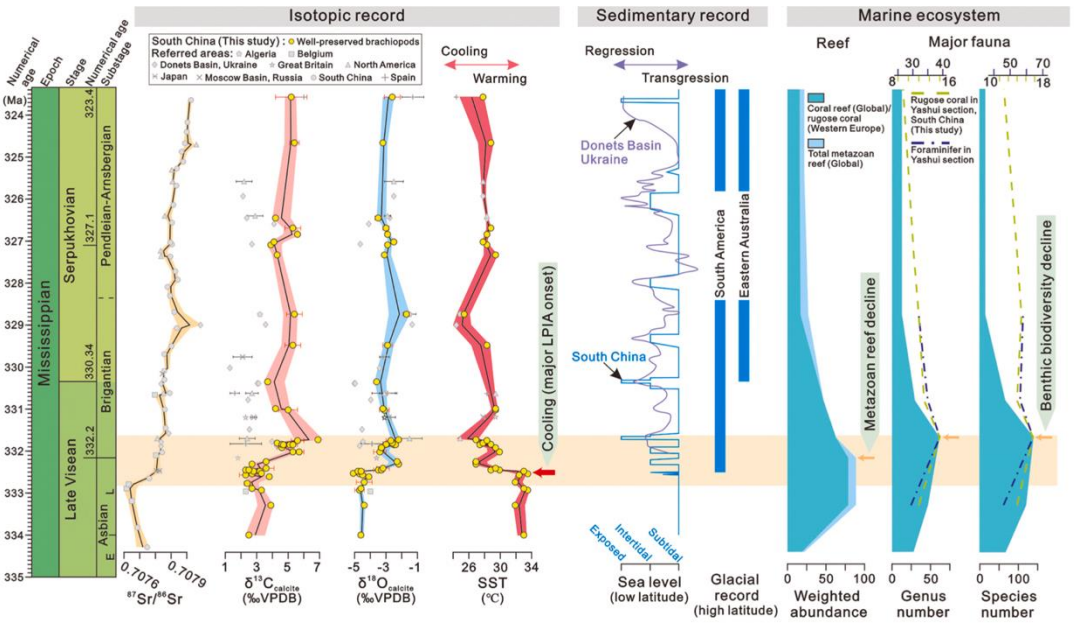

Figure 2. Correlation of isotopic, sedimentary, and marine ecosystem changes from the late Visean

to Serpukhovian. The solid line and shaded area of $^{87}Sr/^{86}Sr$, $\delta^{13}C_{calcite}$, $\delta^{18}O_{calcite}$, and SST represent the LOWESS cure and variation range (±1σ), respectively. The numerical ages are from Aretz et al. (2020). The $^{87}Sr/^{86}Sr$ data are from Brand et al. (2009), Bruckschen et al. (1995, 1999), and Chen et al. (2018). The $\delta^{13}C_{calcite}$ and $\delta^{18}O_{calcite}$ data in yellow (mean value) are from this study, and in gray are from Armend´ariz et al. (2008), Bruckschen et al. (1999), Bruckschen and Veizer (1997), Mii et al. (1999, 2001) and Popp et al. (1986). The SST is reconstructed using the equation in Hays and Grossman (1991). Sea-level profiles are from Chen et al. (2019) and Eros et al. (2012). Glacial records are from Fielding et al. (2008) and Valdez Buso et al. (2020). Metazoan reef abundance and faunal diversity are from Groves et al. (2012) and Yao et al. (2020). The bold, red arrow marks the onset of major phase of LPIA recorded by $\delta^{18}O_{calcite}$ of brachiopods and the thin, tan arrows mark the changes in reefs and benthic fauna. The yellow shaded bar indicates the relationship between isotopic, sedimentary, and marine ecosystem changes during the onset of the main glaciation phase of the LPIA around ~332 Ma. E: Early; L: Late; LPIA: late Paleozoic Ice Age.